International Journal of Nanomedicine

Dovepress
Taylor & Francis Group

Open Access Full Text Article

ORIGINAL RESEARCH

ROS/Glucose-Dissociable EGCG-Coated Oxygen-Supplying Nanocomposite Hydrogel for Diabetic Wound Therapy

Shiyu Sun[1,*], Rongxue Zhu[1,*], Junneng Du[1], Jin Lin[1], Yuying Li[1], Qian Jiang[1], Tianzong Huang[1], Enping Huang[2], Yingping Jiang[1], Xiaoya Zhang[1]

[1]Department of Rehabilitation Medicine, The Affiliated Guangdong Second Provincial General Hospital of Jinan University, Guangzhou, Guangdong, 510310, People's Republic of China; [2]Guangzhou Key Laboratory of Forensic Multi-Omics for Precision Identification, School of Forensic Medicine, Southern Medical University, Guangzhou, Guangdong, 510515, People's Republic of China

*These authors contributed equally to this work

Correspondence: Yingping Jiang; Xiaoya Zhang, Department of Rehabilitation Medicine, The Affiliated Guangdong Second Provincial General Hospital of Jinan University, Guangzhou, Guangdong, 510310, People's Republic of China, Email jyp1104@126.com; 434879599@qq.com

Background: In diabetic wounds, a detrimental and persistent inflammatory environment characterized by impaired angiogenesis and concomitant hypoxia severely impedes wound healing. This study utilized phenylboronic acid-grafted quaternized chitosan (QCS-PBA) to encapsulate calcium peroxide (CaO_2) within the QCS-PBA matrix. Epigallocatechin gallate (EGCG) was then anchored onto the surface via phenylborate ester bonds to fabricate oxygen-producing nanoparticles (QP@Ca-E). Finally, the nanoparticles were integrated into a multifunctional hydrogel (GP-GL) prepared from functionalized gelatin. This system provides a promising therapeutic strategy for irregular wound closure, hypoxia alleviation, inflammatory response modulation, and angiogenesis promotion.

Methods: In this study, QP@Ca-E loaded with CaO_2 and EGCG were combined with functionalized gelatin grafted with double bonds/lipoic acid (GP-GL) to fabricate a photocurable and reactive oxygen species (ROS)-responsive hydrogel delivery system (GP-GL@Ca-E). The system was systematically evaluated for its ROS/glucose-responsive release behavior, antioxidant activity, and antibacterial properties. Through in vitro experiments, the hydrogel's biocompatibility and its effects on cellular ROS/hypoxia levels, angiogenic capacity, and macrophage polarization toward the M2 phenotype were further investigated. Additionally, a full-thickness skin defect model in diabetic rats was established to validate the hydrogel's efficacy in promoting wound healing, restoring oxygen supply, mitigating inflammatory responses, and accelerating angiogenesis.

Results: The GP-GL@Ca-E oxygen-supplying multifunctional hydrogel provides an effective physical barrier for irregular wounds. Moreover, the GP-GL@Ca-E hydrogel responds to ROS and glucose in the wound microenvironment to enable sustained EGCG release. EGCG not only exhibits excellent antibacterial, anti-inflammatory, and antioxidant properties but also promotes angiogenesis. Subsequently, the exposed CaO_2 reacts with water to continuously generate oxygen. The synergistic effect of EGCG and CaO_2 effectively alleviates wound hypoxia and inflammatory responses while promoting neovascularization, thereby creating a favorable microenvironment for diabetic wound repair and significantly accelerating the healing process. In vivo studies confirmed that compared with the control group, the hydrogel-treated group showed significantly accelerated wound healing. By day 14, the wound healing rate reached 99.01% in the hydrogel group, significantly higher than the 86.32% observed in the control group, fully demonstrating its great potential for diabetic wound therapy.

Conclusion: The results indicate the successful preparation of a multifunctional oxygen-producing hydrogel, which exhibits remarkable antibacterial properties and ROS scavenging capability. This hydrogel can effectively suppress inflammatory responses, promote macrophage polarization toward the M2 phenotype, and enhance angiogenesis, thereby creating a favorable immune microenvironment for skin regeneration. These characteristics collectively demonstrate its promising potential for application in diabetic wound healing.

Keywords: oxygen production, ROS/glucose-dissociable, EGCG-coated, diabetic wound therapy

Received: 26 July 2025
Accepted: 9 October 2025
Published: 23 October 2025

Graphical Abstract

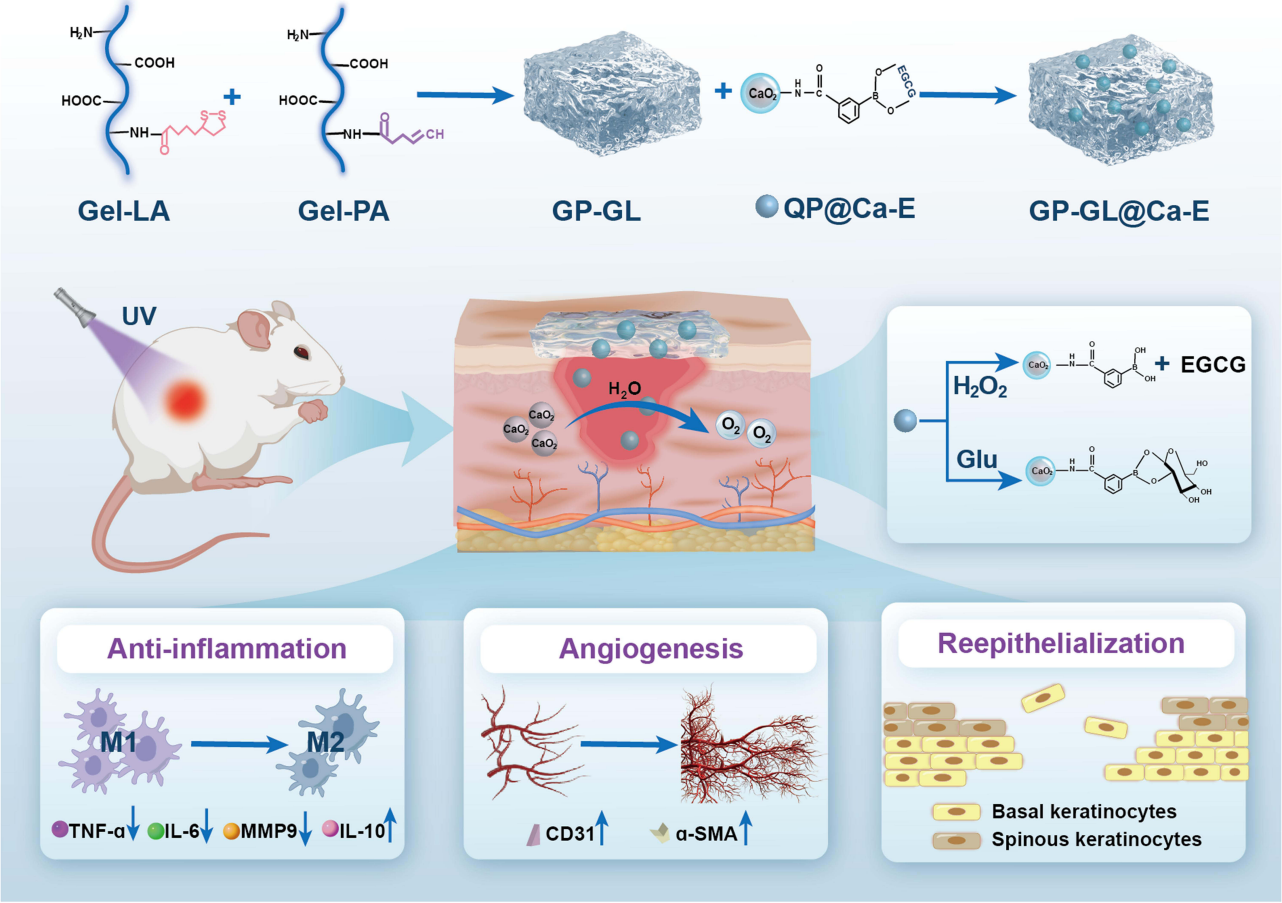

Introduction

Diabetic wounds, among the most prevalent complications of diabetes, impose a substantial burden on both patients and society.[1,2] They are characterized by impaired angiogenesis, chronic inflammation, and diminished tissue regeneration capacity.[3–5] Despite significant advances in wound care techniques and therapeutic approaches, the clinical outcomes for diabetic wounds remain suboptimal. This challenge primarily stems from the complex wound microenvironment, where factors such as hyperglycemia, excessive inflammation, hypoxia, and oxidative stress collectively impede the repair and healing processes.[6,7] Wound healing normally progresses through four distinct phases: hemostasis, inflammation, tissue formation, and tissue remodeling.[8] However, in diabetic wounds, hyperglycemia-induced vasculopathy and persistent inflammatory responses disrupt this progression, leading to chronic, non-healing wounds.[9,10] Oxidative stress, induced by chronic inflammation, causes reactive oxygen species (ROS) to accumulate. This ROS accumulation damages healthy cells and the microvasculature in deeper tissues,[11–13] further exacerbating the chronic hypoxic state characteristic of diabetic wounds.[14] Hypoxia suppresses cellular self-repair mechanisms against organelle and functional decay, and disrupts the maintenance of calcium ion concentrations required for ATP-dependent cellular functions. Prolonged tissue exposure to hypoxic conditions ultimately triggers apoptosis and necrosis.[15] Consequently, strategies aimed at modulating blood glucose levels and inflammatory responses to ameliorate the wound microenvironment, alleviate oxidative stress and hypoxia, represent highly promising therapeutic approaches for diabetic wound management.

To counteract the prevalent hypoxia that impedes wound healing, CaO_2 emerges as a highly promising oxygen-generating agent.[16] Its reaction with water enables sustained O_2 release, directly alleviating local hypoxia and creating

a more favorable microenvironment essential for cell activities involved in repair and regeneration.[17] Bankar et al[18] utilized CaO_2 nanoparticles to generate oxygen, disrupting the anaerobic conditions within oral bacterial biofilms and thereby enhancing antibiotic efficacy. Jia et al[19] employed CaO_2 to produce both O_2 and H_2O_2, addressing the limitation in ROS therapeutic efficacy imposed by oxygen substrate scarcity during tumor treatment. However, the rapid hydrolysis of CaO_2 in the physiological environment not only leads to an unsustainable burst release of oxygen but also generates strongly alkaline by-products that cause severe damage to cells and tissues. Consequently, modifications to CaO_2 are necessary, aiming to precisely regulate its hydrolysis kinetics. This strategy seeks to maximize its efficient oxygen supply capacity while minimizing the associated risks of cytotoxicity and tissue damage. Nevertheless, diabetic wound healing represents a complex, multi-factorial process involving multiple stages. A single oxygen-supply strategy often proves inadequate to address its multifaceted pathological barriers, including oxidative stress and persistent inflammation.

To mitigate oxidative stress damage and persistent inflammation, reductive agents such as natural small-molecule compounds, exosomes, and nanozymes are commonly employed. Epigallocatechin gallate (EGCG), a potent natural polyphenol derived from green tea, exhibits exceptional antioxidant properties, effectively scavenging excess ROS and alleviating oxidative damage.[20] Furthermore, EGCG exerts anti-inflammatory effects by modulating macrophage polarization, thereby suppressing chronic inflammation in diabetic wounds.[21] Despite demonstrating therapeutic potential, the direct application approach struggles to achieve precise, targeted delivery of antioxidants to high-ROS regions within the wound. Consequently, constructing an integrated multifunctional smart delivery platform—capable of efficient antioxidation, anti-inflammation, and oxygen generation—holds significant promise for overcoming the limitations of monotherapies and achieving synergistic therapeutic outcomes. The in situ-forming hydrogel can overcome the limitations imposed by wound irregularity, perfectly adapting to wounds of varying sizes, shapes, and depths to provide an effective physical barrier.[22]

Effective diabetic wound therapy requires a dual capability of supplying oxygen and scavenging ROS to minimize the need for repeated treatments. To overcome these critical limitations, this study developed a ROS/glucose-responsive and oxygen-supplying nanocomposite hydrogel coated with EGCG. The hydrogel was fabricated through UV-initiated cross-linking of double bond-modified gelatin (GP) and lipoic acid (LA)-modified gelatin (GL). To achieve sustained oxygen release and prevent the burst release of oxygen upon contact of CaO_2 with the moist wound environment, we encapsulated CaO_2 nanoparticles using quaternized chitosan grafted with phenylboronic acid groups (QCS-PBA). Subsequently, EGCG was anchored onto the QCS-PBA surface via dynamic boronate ester bonds, forming QP@Ca-E nanoparticles, which were ultimately loaded into the hydrogel network. As illustrated in Figure 1, the diabetic wound microenvironment is characterized by hyperglycemia and elevated oxidative stress. The boronate ester bonds within the QP@Ca-E nanoparticles exhibit dual responsiveness to ROS and glucose, enabling the triggered release of EGCG specifically within the wound microenvironment. Concurrently, CaO_2 reacts with water to generate a sustained supply of oxygen, alleviating local hypoxia. Complementing this, the released EGCG exerts its potent antioxidant and anti-inflammatory effects, effectively scavenging ROS, mitigating oxidative stress damage, and promoting angiogenesis. Thus, the combined actions of CaO_2 and EGCG establish a positive feedback pathway: Alleviation of hypoxia and oxidative stress modulates the inflammatory response, rebalancing the wound immune microenvironment, thereby accelerating diabetic wound healing.

Methods and Materials

Materials

Calcium chloride dihydrate ($CaCl_2 \cdot 2H_2O$, AR), sodium hydroxide (NaOH, AR), hydrogen peroxide (H_2O_2, AR), quaternized chitosan (QCS, AR), 2-formylphenylboronic acid (FPBA, AR), epigallocatechin gallate (EGCG, AR), 4-pentenoic acid (PA, AR), lipoic acid (LA, AR), and bovine bone-derived gelatin (Gel, AR) were purchase from Macklin, N-hydroxysuccinimide (NHS, AR), 1-ethyl-(3-dimethylaminopropyl) carbodiimide (EDC, AR) were purchased from Aladdin. Lipopolysaccharide (LPS) was obtained from Sigma-Aldrich (St. Louis, MO, USA). Mouse macrophage cells (RAW264.7) and human umbilical vein endothelial cells (HUVEC) were procured from Procell Life Science & Technology Co., Ltd. (Wuhan, China). Calcein/PI Cell Viability and Cytotoxicity Assay Kit, Cell Counting Kit-8 (CCK-8), and 2′,7′-Dichlorodihydrofluorescein diacetate (DCFH-DA) Assay Kit (Beyotime Biotechnology, Shanghai, China), alongside the Cell Hypoxia Detection Kit [$Ru(dpp)_3Cl_2$] (BIOESN, Shanghai, China). Staining reagents included Hoechst and DAPI staining solutions, as well as an FITC-labeled

 https://doi.org/10.2147/IJN.S556446

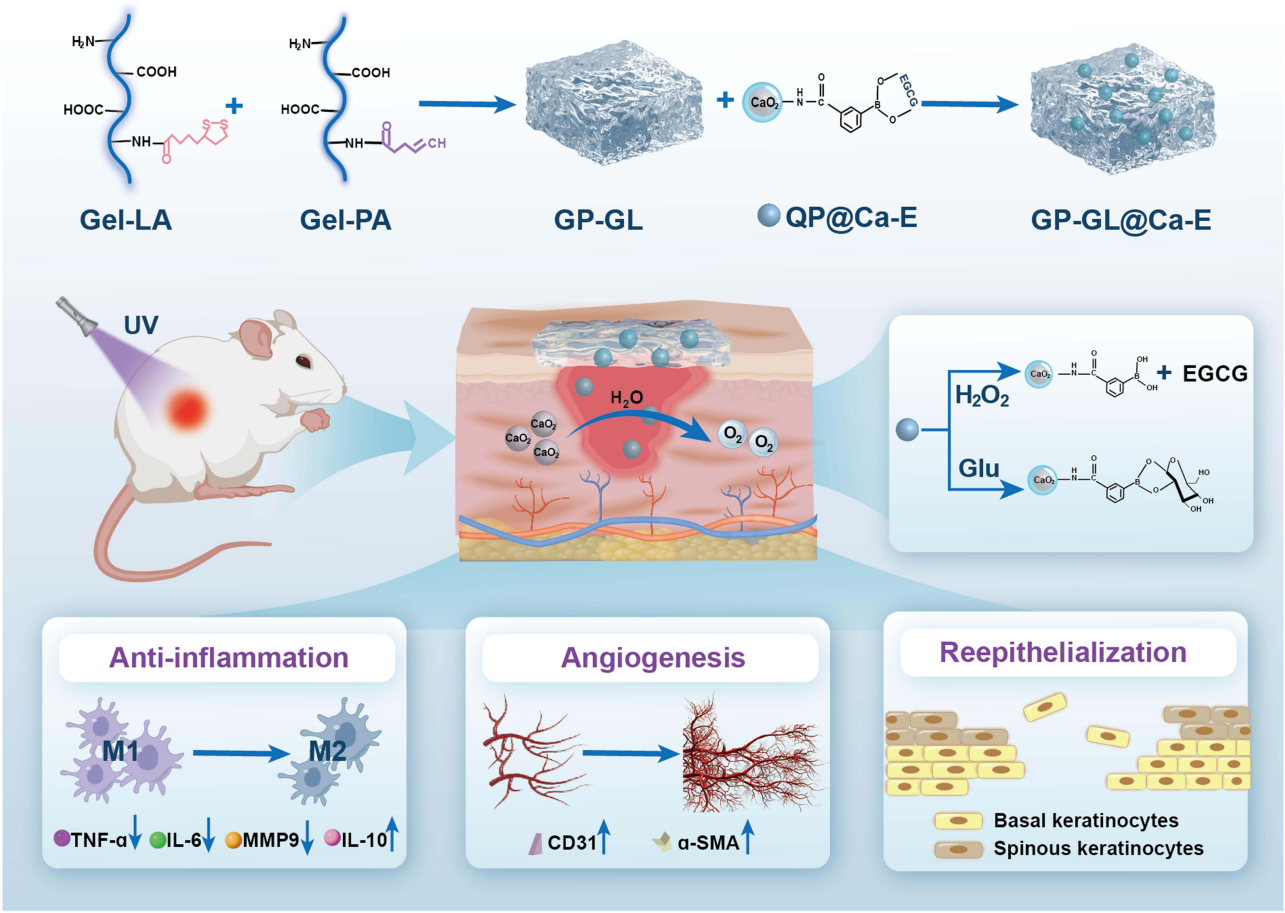

Figure 1 Preparation of GP-GL@Ca-E oxygen-supplying nanocomposite hydrogel and its underlying mechanisms in mediating diabetic wound healing.

phalloidin staining kit (Solarbio, Beijing, China). Antibody sources were as follows: PE/Cy7 anti-mouse CD206 and FITC anti-mouse CD86 (Proteintech, Wuhan, China) for immunofluorescence; interleukin-6 (IL-6), matrix metalloproteinase-9 (MMP9), tumor necrosis factor-alpha (TNF-α), and interleukin-10 (IL-10) antibodies (Abcam, Cambridge, UK) for immunohistochemical.

Synthesis of CaO_2 NPs

Aqueous $CaCl_2 \cdot 2H_2O$ solution (53 g in 200 mL distilled water) was prepared via 15-min ultrasonication. Upon complete dissolution, 80 mL of 1 M NaOH was added dropwise during continuous magnetic stirring (350 rpm, 30 min). The reaction system then received dropwise addition of 100 mL 10 mM H_2O_2 solution with sustained stirring for 2 h. This process generated a milky white suspension, confirming CaO_2 NPs formation through gradual precipitation. The NPs were collected by centrifugation, purified through sequential washing with NaOH solution and distilled water, and dried at 80 °C for 2 h. The resultant solid was mechanically triturated in an agate mortar to yield a fine homogeneous powder.

Synthesis of QP@Ca-E Nanoparticles

Synthesis of QCS-FPBA

1.0 g QCS was dissolved in 100 mL of distilled water. After adding 25 mg EDC and 20 mg NHS, the solution was activated for 30 min. Subsequently, 200 mg FPBA was introduced into the reaction mixture. The conjugation reaction proceeded under magnetic stirring (350 rpm) at room temperature for 24 h. The resulting QCS-FPBA conjugate was isolated by lyophilization.

Synthesis of QCS-FPBA@CaO_2-EGCG (QP@Ca-E)

QP@Ca-E nanocomposites were synthesized by dissolving QCS-FPBA (100 mg) in distilled water (40 mL), followed by introducing CaO_2 nanoparticles (100 mg). After 3 h of room-temperature stirring, the mixture underwent centrifugation with supernatant removal. The collected solid was re-dispersed in fresh distilled water (40 mL), and epigallocatechin gallate (EGCG, 20 mg) was incorporated. The reaction proceeded under continuous stirring at ambient temperature for 4 h. The final product, denoted QCS-FPBA@CaO_2-EGCG (QP@Ca-E), was isolated by lyophilization.

Hydrogel Preparation

Synthesis of Gelatin Grafted with 4-Pentenoic Acid (GP)

4-Pentenoic acid (PA, 210 mg) was activated in deionized water (10 mL) using EDC (146 mg) and NHS (108 mg) under 1 h room-temperature stirring. The activated PA solution was then slowly introduced into ice-cooled 2% (w/v) gelatin solution, followed by 6 h continuous reaction. The product was dialyzed (3 days, distilled water) and lyophilized to yield GP.

Synthesis of Gelatin Grafted with Lipoic Acid (GL)

Lipoic acid (LA, 420 mg) underwent identical activation in DMSO (10 mL) with EDC (68 mg) and NHS (50 mg). The solution was similarly reacted with ice-cooled 2% gelatin solution for 6 h. Subsequent dialysis (3 days) and lyophilization afforded GL.

UV-Induced Crosslinking for Gel Formation (GP-GL)

The GP-GL hydrogel was fabricated by homogenizing GP and GL (1:1, w/w) with Irgacure 2959 (0.1 wt% of gel precursors) prior to UV-induced crosslinking.

Material Characterization

Characterization of QP@Ca-E Nanoparticles

QP@Ca-E nanoparticles were structurally characterized using Fourier-transform infrared spectroscopy (FTIR, SHIMADZU IRTracer-100, Japan; 400–4000 cm^{-1} range) to analyze functional groups in QCS, FPBA, QCS-FPBA, EGCG, and QP@Ca-E. Grafting efficiency was determined via ^1H nuclear magnetic resonance spectroscopy (^1H NMR, Bruker AVANCE III HD 600, Germany). Morphological features and elemental distribution were examined by transmission electron microscopy (TEM, JEOL JEM-F200, Japan) with energy-dispersive X-ray spectroscopy (EDS), while hydrodynamic diameter and surface charge were quantified via dynamic light scattering (Malvern Panalytical Zetasizer Pro, UK).

Characterization of Hydrogels

For hydrogels, FTIR and ^1H NMR (same instruments) elucidated chemical compositions of Gel, PA, LA, Gel-PA (GP), and Gel-LA (GL). Microstructural architecture was probed using scanning electron microscopy (SEM, ZEISS Sigma 360, Germany) on lyophilized specimens.

Oxygen Release

The dissolved O_2 concentration in aqueous solution was monitored using a portable dissolved oxygen meter. To evaluate the catalytic capability of QP@Ca-E, the nanoparticles were co-incubated with H_2O_2 (10 mM), and O_2 generation was measured at different time intervals, with CaO_2 serving as the control. Real-time monitoring of O_2 concentration was performed using an oxygen microsensor (OX-NP, Unisense A/S, Denmark), with the probe immersed directly into the reaction solution.

In vitro Drug Release Study

Identical hydrogel specimens were immersed in 10 mL solutions containing gradient concentrations of H_2O_2, glucose, or PBS, followed by orbital shaking incubation (37 °C, 100 rpm). At defined intervals, 2 mL aliquots of release medium were collected and replenished with fresh buffer. EGCG release kinetics were quantified by UV-Vis spectrophotometry, with cumulative release derived from pre-calibrated standard curves.

Antioxidant and Antibacterial Properties of GP-GL@Ca-E

Hydrogel antioxidant capacity was quantified via DPPH radical scavenging assay (BC4750, Solarbio, Beijing) per manufacturer specifications. For antibacterial assessment, standardized hydrogel samples were immersed in *E. coli* and *S. aureus* suspensions under orbital incubation (37 °C, 100 rpm). Bacterial growth kinetics were tracked by monitoring OD_{620} at 2-h intervals. Quantitative evaluation involved 8-h co-culture, serial dilution to 10^6, and plating 100 μL aliquots on LB agar. After 24-h incubation (37 °C), antibacterial efficacy was determined by colony-forming unit (CFU) enumeration.

In vitro Cell Experiments

1 mL GP-GL@Ca-E with nanoparticles concentration of 1 mg/mL were immersed in 48 mL of complete cell medium. Gel extracts were used for subsequent cell experiments.

Cell Viability

HUVEC proliferation responses to hydrogel extracts were assessed using three formulations: GP, GP-GL, and GP-GL @Ca-E. Cells were seeded in 96-well plates (1×10^6 cells/well) and exposed to extracts for 24/48 h. Viability was quantified via CCK-8 assay, with live/dead staining providing fluorescence microscopic visualization of cell status.

Cytoskeleton Staining

Following 24-h co-culture with hydrogel extracts, HUVECs underwent PBS washing, fixation in 4% paraformaldehyde (20 min, RT), and sequential staining: FITC-phalloidin (1 h) for actin visualization and DAPI (10 min) for nuclear labeling. Cytoskeletal architecture was examined by confocal laser scanning microscopy.

ROS Scavenging and Oxygen Generation

HUVECs (1×10^4 cells/well) were cultured in 6-well plates with either hydrogel-coated or uncoated surfaces. Following hypoxia/high glucose (HG) induction, cells were sequentially stained with the ROS probe DCFH-DA and the hypoxia detection probe $Ru(dpp)_3Cl_2$. Intracellular ROS levels and hypoxic status were assessed using fluorescence microscopy.

Tube Formation Assay

Matrigel (50 μL/well, Beyotime) was deposited into 24-well plates and polymerized at 37 °C. HUVECs (2×10^4 cells/well) were seeded onto the gelled matrix and cultured overnight. Following hypoxia/high-glucose exposure, hydrogel extracts were introduced for 4 h incubation. Endothelial tube formation was then documented by optical microscopy.

Scratch Wound Assay

Confluent HUVEC monolayers (seeded at 1×10^6 cells/well in 6-well plates) underwent hypoxia/high-glucose treatment. A sterile 200 μL pipette tip was used to create a uniform scratch. Reference points at scratch/reference line intersections were monitored. Following debris removal with three PBS washes, hydrogel extracts were added. Optical microscopy captured wound images at 0, 24, and 48 h. ImageJ software quantified the wound healing area.

Transwell Migration Assay

Serum-starved cells (in basal medium) were seeded onto the upper chambers of Corning 12-well Transwell inserts (8 μm pore). The lower wells received three different hydrogel extracts. After 24 h incubation, non-migrated cells on the upper chamber membrane were removed by swabbing. Migrated cells adherent to the lower membrane underwent fixation (4% paraformaldehyde, 37 °C, 30 min), PBS washing, staining with 0.5% crystal violet, and visualization under an inverted microscope.

Immunofluorescence Analysis

Cells were PBS-rinsed and fixed in 4% paraformaldehyde (30 min). After permeabilization with 0.1% Triton X-100 (10 min), nonspecific sites were blocked with BSA (1 h, RT). Overnight incubation at 4 °C with fluorescent primary antibodies against CD86 and CD206 (Proteintech; both 1:200) was followed by PBS washes, DAPI nuclear counterstaining, and fluorescence microscopy imaging.

Quantitative Real-Time PCR (qRT-PCR)

TRIzol-extracted RNA from hydrogel-treated HUVECs was reverse-transcribed to cDNA (FastKing RT kit; Tiangen, China). qPCR used SYBR Green Mix (FastReal qPCR PreMix; Tiangen, China) on a Roche Lightcycler 96 system with the primers (Table 1).

In vivo Diabetic Wound Healing Model

The animal study was reviewed and approved by the Institutional Animal Care and Use Committee (IACUC) of Guangdong Second Provincial General Hospital (Approval No. 2024-DW-KZ-143-02). All procedures were performed in compliance with the Chinese National Standard GB/T 35892–2018 "Guideline for Welfare and Ethical Review of Laboratory Animals to ensure the welfare of laboratory animals". The reporting of this study follows the ARRIVE guidelines. Diabetic SD rats (8-week-old) were induced by 60 mg/kg STZ intraperitoneal injection. Hyperglycemia (>16.7 mmol/L at 1 week) confirmed successful modeling. Dorsal full-thickness wounds (15 mm diameter) were created and divided into four groups: Control, GP, GP-GL, GP-GL@Ca-E. In the in vivo animal experiments, we applied 2 mL of GP-GL@Ca-E with nanoparticle concentration of 1mg/mL to treat diabetic wounds. Wounds were photographed on days 0, 3, 5, 7, 9, 14.

For histology/IHC: Rats were euthanized, and wound tissues fixed in 4% PFA, paraffin-embedded, and sectioned (4 μm). H&E and Masson staining used Solarbio kits. IHC sections incubated overnight (4 °C) with anti-IL-6/MMP9/TNF-α/IL-10 (1:200; Abcam), followed by secondary antibodies and DAB. Nuclei counterstained, sections resin-mounted.

For immunofluorescence: Sections incubated with anti-CD31/α-SMA (1:200; Abcam) overnight (4 °C), treated with fluorescent secondary antibodies, nuclei stained, and imaged by fluorescence microscopy.

Statistical Analysis

Data were analyzed using SPSS 26.0 (IBM, USA) and graphed with Origin 2021 (OriginLab, USA), presented as mean ± SD. Statistical significance (*$p < 0.05$, **$p < 0.01$, *$p < 0.001$) was evaluated by one-way ANOVA or Student's *t*-test.

Table 1 Primer List for qPCR

Gene Name	Primer (5′–3′)
Gapdh	CGGACCAATACGACCAAATCCG
	AGCCACATCGCTCAGACACC
Inos	CTACCTACCTGGGGAACACCTGGG
	GGAGGAGCTGATGGAGTAGTAGCGG
Arg-1	GCTGTGGTAGCAGAGACCCAGA
	CATCCACCCAAATGACGCATAG
Ccl2	CAGGTCTCTGTCACGCTTCT
	AGTATTCATGGAAGGGAATAG
Cxcl2	TCCTCAATGCTGTACTGGTCC
	ATGTTCTTCCTTTCCAGGTC

Abbreviations: *Gapdh*, glyceraldehyde-3-phosphate dehydrogenase; *Inos*, inducible nitric oxide synthase; *Arg-1*, arginase 1; *Ccl2*, C-C motif chemokine ligand 2; *Cxcl2*, C-X-C motif chemokine ligand 2.

https://doi.org/10.2147/IJN.S556446

Results and Discussion

Characterization of QP@Ca-E Nanoparticles

QP@Ca-E nanoparticles with oxygen-generating capacity were fabricated by first synthesizing CaO_2 using established methods. QCS was then grafted with 2-formylphenylboronic acid via amide reaction to form QCS-FPBA. Subsequently, QCS-FPBA was used to encapsulate CaO_2 to yield QP@CaO_2, followed by conjugation with EGCG to generate the final nanoparticles. FTIR spectroscopy confirmed successful phenylboronic acid grafting onto QCS (Figure 2A), evidenced by the characteristic B-O absorption peak at 1126 cm^{-1}. ^1H NMR analysis further validated this modification (Figure 2B), showing proton peaks at 7.49–7.89 ppm corresponding to the phenyl ring. The FTIR spectrum of QP@Ca-E nanoparticles (Figure 2C) exhibited a prominent peak at 1458 cm^{-1}, assigned to the C=C stretching vibrations of the aromatic

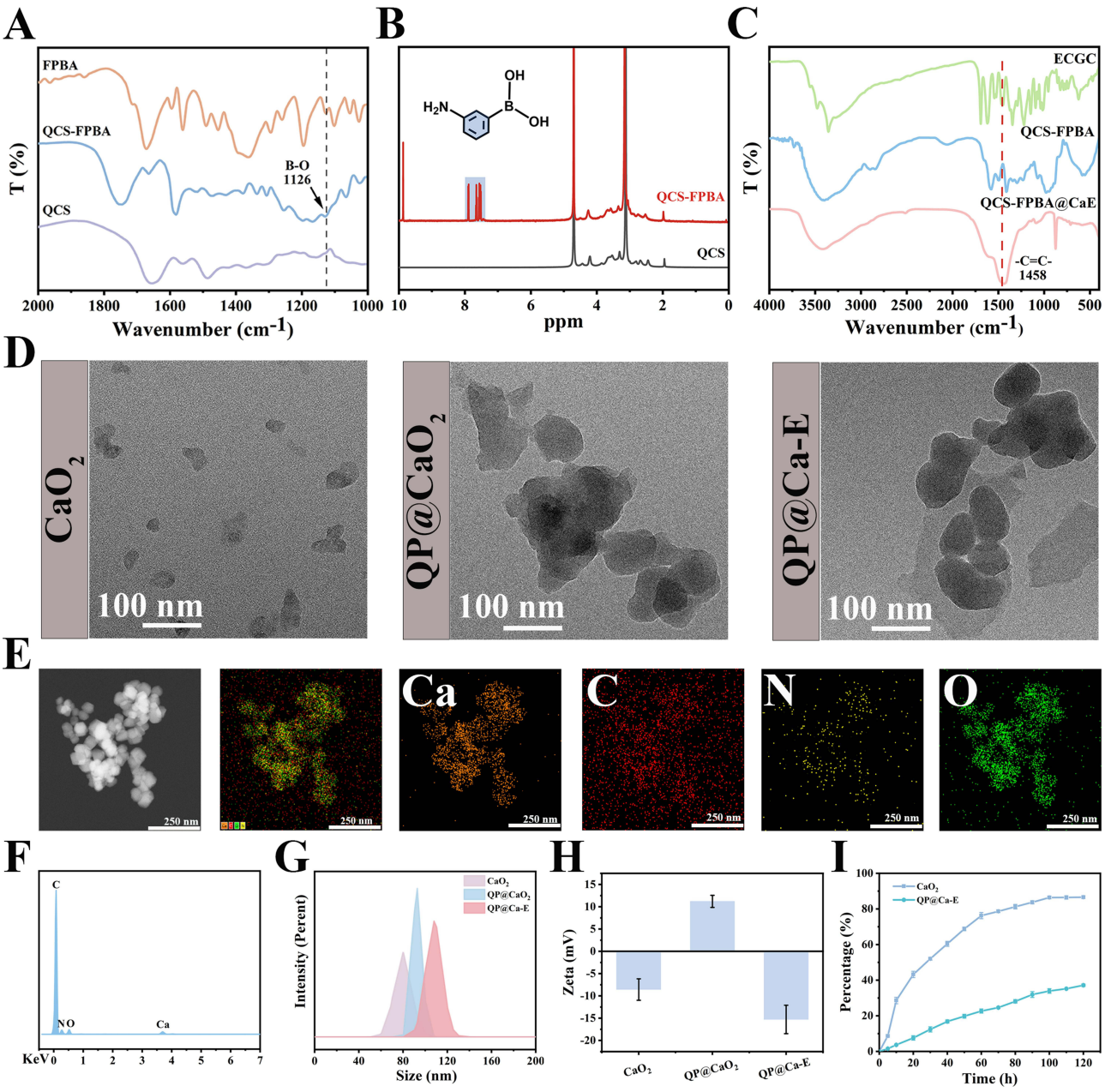

Figure 2 Characterization of QP@Ca-E. (**A**) FT-IR spectrum of QCS-FPBA. (**B**) ^1H NMR spectrum of QCS-FPBA. (**C**) FT-IR spectrum of QP@Ca-E. (**D**) TEM images of CaO_2, QP@CaO_2, and QP@Ca-E. (**E**) Elemental mapping images and (**F**) EDS spectrum of QP@Ca-E. (**G**) Particle size and (**H**) zeta potential of CaO_2, QP@CaO_2, and QP@Ca-E. (**I**) Oxygen release profiles of CaO_2 and QP@Ca-E.

rings in EGCG, confirming successful nanoparticle synthesis. TEM revealed that both CaO_2 and QP@CaO_2 particles exhibited diameters of approximately 50 nm, while the diameter of QP@Ca-E exceeded 100 nm after conjugation with EGCG (Figure 2D). Elemental mapping (Figure 2E) and energy-dispersive X-ray spectroscopy (EDS) (Figure 2F) demonstrated the homogeneous distribution of Ca, C, N, and O within the nanoparticles. The presence of the Ca element confirmed the successful fabrication of the QP@Ca-E nanoparticles. Dynamic light scattering confirmed progressive size increase following QP encapsulation and EGCG grafting (Figure 2G). Zeta potential analysis (Figure 2H) indicated charge reversal from negative (CaO_2) to positive (QP@CaO_2) due to quaternary ammonium groups, while subsequent EGCG conjugation restored negative potential through boronic ester bond formation and phenolic hydroxyl dissociation. Oxygen release profiles demonstrated that CaO_2 exhibited faster release kinetics than QP@Ca-E, with the latter sustaining oxygen generation for >5 days (Figure 2I). This confirms that QP encapsulation effectively mitigates the initial burst release of oxygen and modulates the release kinetics, prolonging oxygen delivery. Specifically, by day 5, the oxygen release rate reached >80% for unencapsulated CaO_2, while QP@ CaO_2 (the core component of QP@Ca-E) exhibited a significantly lower rate of only 37.16%. Meanwhile, the experiment also investigated the changes in pH during the oxygen generation process (Figure S4). The early increase in pH may be attributed to the reaction between CaO_2 and water, producing $Ca(OH)_2$. Meanwhile, H_2O_2 promotes the release of EGCG, which upon oxidation generates acidic products. In addition, H_2O_2 oxidizes and degrades gelatin, producing a large number of small molecular peptides and amino acid fragments. These fragments expose more carboxyl terminals (–COOH) and oxidatively generated carboxyl groups, ultimately leading to the accumulation of acidic groups in the system and a subsequent decrease in pH. Collectively, these results verify the successful synthesis of oxygen-generating QP@Ca-E nanoparticles.

Characterization of GP-GL@Ca-E Hydrogels

UV-crosslinkable gelatin was synthesized by grafting 4-pentenoic acid onto gelatin (GP) via an amidation reaction. Similarly, LA was grafted onto Gel to yield GL. The grafting efficiencies for both modifications were verified by ^{1}H NMR and FTIR spectroscopy. The ^{1}H NMR spectrum of GP (Figure 3A) exhibited a characteristic peak at 5.77 ppm, corresponding to the vinyl protons. FTIR analysis (Figure 3B) revealed that after double-bond grafting, the -NH_2 peak of gelatin (3432 cm^{-1}) shifted to the amide -NH- (3530 cm^{-1}). Additionally, the sharp peak of PA at 1645 cm^{-1} broadened in GP due to the influence of -C=C-. These results confirmed the successful synthesis of GP. Similarly, the ^{1}H NMR spectrum of GL (Figure 3C) displayed peaks at 3.13 ppm (protons of the five-membered ring) and 1.4 ppm (aliphatic protons). FTIR spectra (Figure 3D) showed the presence of amide -NH- (1544 cm^{-1}) and disulfide -S-S- (670 cm^{-1}) stretching vibrations, indicating the successful preparation of GL. After adding photoinitiator I2959 to GP and GP-GL, respectively, hydrogels were formed under UV irradiation, and their microstructures were examined by SEM. Both GP and GP-GL hydrogels exhibited highly porous three-dimensional structures (Figure 3E). However, the pore size of the GP-GL hydrogel was smaller than that of the GP hydrogel, indicating that the introduction of multiple crosslinking resulted in denser and tighter crosslinking in GP-GL. Mapping also revealed the uniform distribution of nanoparticles in GP-GL@Ca-E (Figure S2). Given the ROS-responsive properties of the boronic ester bonds in QP@Ca-E nanoparticles and the disulfide bonds within the hydrogel (Figure 3F), we investigated the EGCG release profile from the nanoparticles in the presence of H_2O_2. According to the EGCG standard curve determined by UV-vis absorption spectroscopy, the loading rate of EGCG can be calculated to be 4.5% (Figure S1). First, the release behavior of EGCG from the hydrogel-embedded nanoparticles under different H_2O_2 concentrations was evaluated. As shown in Figure 3G, the cumulative release of EGCG increased with rising H_2O_2 concentration, exceeding 80% at 10 mM H_2O_2. Furthermore, Figure 3H demonstrated that QP@Ca-E nanoparticles exhibited significantly enhanced EGCG release under high glucose conditions compared to PBS, indicating their glucose-responsive characteristics. These results confirm that the ROS/glucose dual-responsive hydrogel was successfully prepared.

Antioxidant and Antibacterial Properties of GP-GL@Ca-E Hydrogels

Oxidative stress exacerbates inflammation and impairs wound healing, underscoring the importance of hydrogel dressings with robust antioxidant capabilities. DPPH assays assessed hydrogel free radical scavenging. Control and GP groups showed distinct 517 nm UV peaks (Figure 4A), indicating significant unquenched DPPH radicals. Quantitative

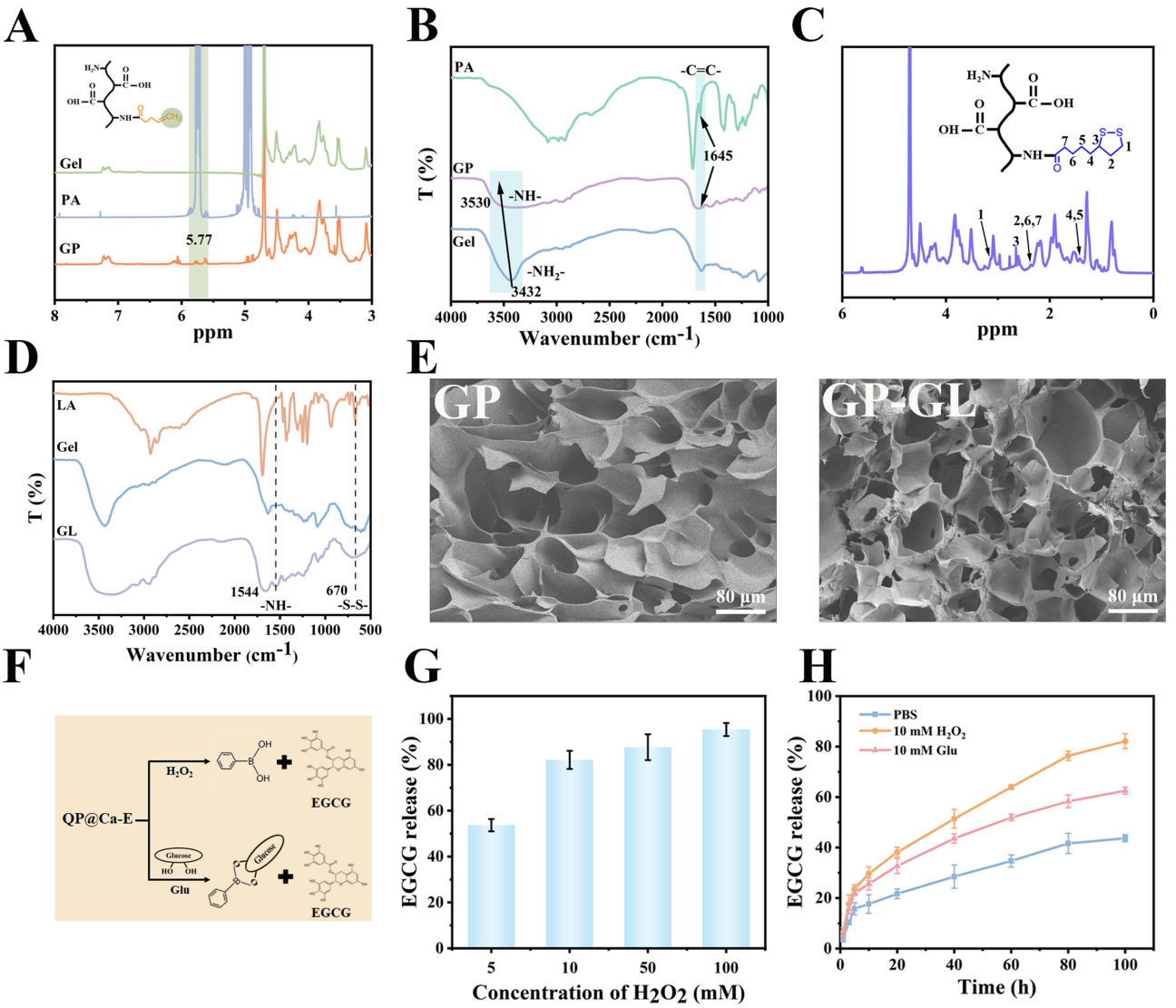

Figure 3 Characterization of GP-GL@Ca-E hydrogels. (**A**) ^{1}H NMR spectra of gelatin, 4-pentenoic acid, and GP. (**B**) FT-IR spectra of gelatin, 4-pentenoic acid, and GP. (**C**) ^{1}H NMR spectrum of GL. (**D**) FT-IR spectra of gelatin, lipoic acid, and GL. (**E**) SEM image of the GP hydrogel and GP-GL hydrogel. (**F**) Schematic representation of ROS/glucose release in response to QP@Ca-E. (**G**) Cumulative EGCG release rate from GP-GL@Ca-E hydrogels incubated with H_2O_2 at varying concentrations. (**H**) Cumulative EGCG release rate from GP-GL@Ca-E hydrogels incubated in PBS, H_2O_2, and glucose solutions.

analysis revealed that the radical scavenging rates of GP, GP-GL, and GP-GL@Ca-E were 9.07 ± 3.20%, 51.02 ± 9.22%, and 80.98 ± 3.40% (Figure 4B), respectively. The superior scavenging ability of GP-GL over GP arose from the grafted lipoic acid (in GL), a potent antioxidant. Further enhancement was observed in GP-GL@Ca-E, where the incorporation of EGCG-loaded nanoparticles (QP@Ca-E) contributed to its exceptional antioxidant performance, owing to EGCG's well-documented radical-neutralizing effects. The hyperglycemic environment in diabetic wounds increases susceptibility to bacterial infections, necessitating antimicrobial functionality in ideal wound dressings. To assess this, hydrogels were co-cultured with *E. coli* and *S. aureus*, and bacterial growth curves were plotted by monitoring OD over time. Figure 4C (*E. coli*) and 4D (*S. aureus*) demonstrated consistent trends: while GP and Control groups showed negligible antibacterial activity, both GP-GL and GP-GL@Ca-E suppressed bacterial proliferation, with the latter exhibiting more pronounced inhibition. Colony counting assays (Figure 4E) further confirmed the significant antibacterial efficacy of GP-GL@Ca-E against both pathogens. These results collectively demonstrate that GP-GL@Ca-E hydrogels possess excellent antioxidant and antibacterial properties.

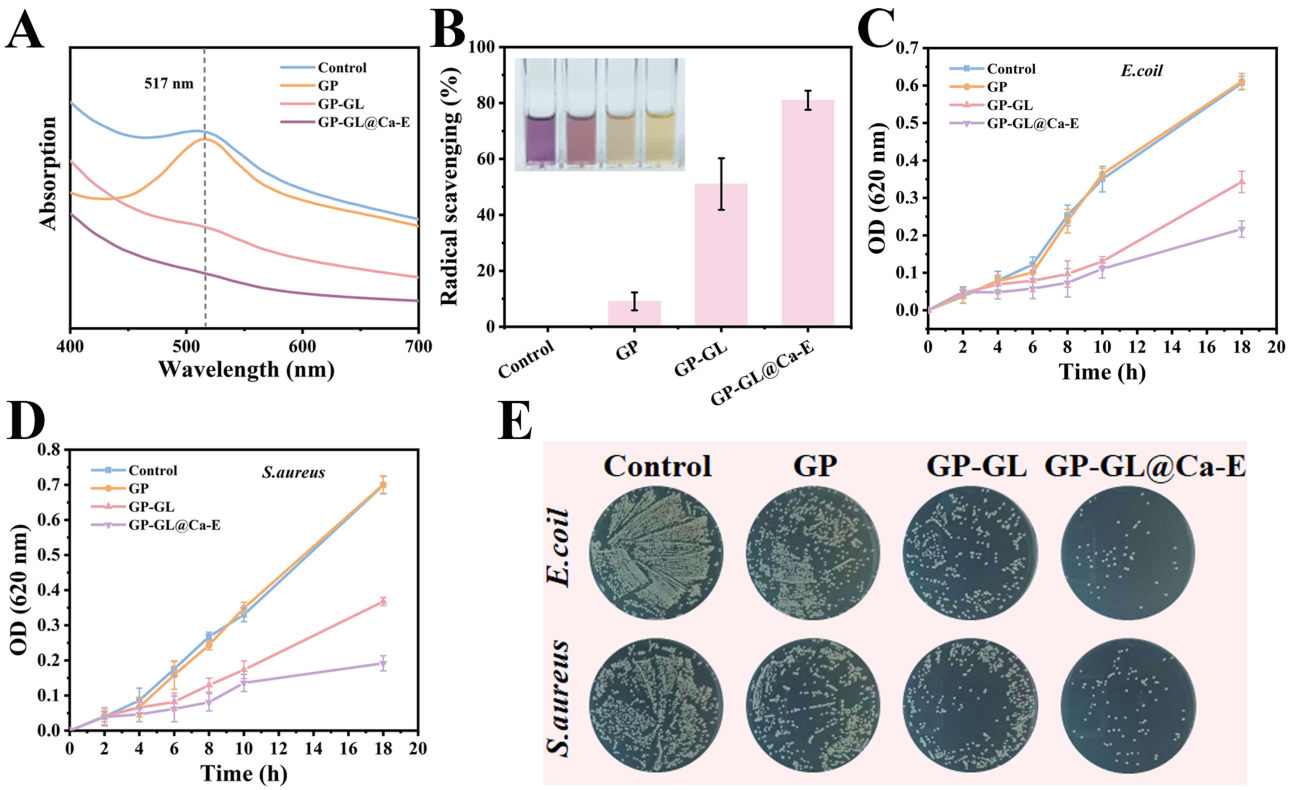

Figure 4 Antioxidant and antibacterial properties of GP-GL@Ca-E hydrogels. (**A**) UV absorption curves depicting DPPH radical scavenging by different-component hydrogels. (**B**) Photograph illustrating DPPH radical scavenging and corresponding quantitative analysis of radical scavenging capacity for different-component hydrogels. Bacterial growth curves of (**C**) *E. coli* and (**D**) *S. aureus*. (**E**) Plate photographs evaluating the antibacterial activity of different-component hydrogels against *E. coli* and *S. aureus*.

Biocompatibility of GP-GL@Ca-E Hydrogels

Biocompatibility is critical for wound dressing clinical translation.[23] Hydrogel extracts were incubated with HUVECs for 24/48 h, then assessed via CCK-8 assays and live/dead staining. The live/dead staining results (Figure 5A) demonstrated that hydrogel extracts did not compromise cell viability, with the majority of cells exhibiting green fluorescence (live cells). CCK-8 data further revealed that after 24 h and 48 h of culture, HUVECs exposed to extracts from all hydrogel groups maintained viability exceeding 100%. Notably, hydrogels containing EGCG significantly enhanced cell proliferation (Figure 5B). To examine cellular morphology, actin filaments were visualized using phalloidin staining. HUVECs exposed to hydrogel extracts exhibited organized cytoskeletal bundles and networks (Figure 5C). Furthermore, hydrogel extracts promoted an increase in cell spreading area (Figure 5D). To simulate diabetic physiological conditions in vitro, cells were subjected to hypoxia and high glucose (HG) treatment. Post-HG injury, cells incubated with hydrogels underwent viability assessment (live/dead staining, CCK-8). Live/dead staining (Figure 5E) showed significantly fewer live cells and elevated dead cells (red fluorescence) in model group. However, treatment with hydrogels gradually restored cell viability, a trend corroborated by quantitative CCK-8 results (Figure 5F). These findings collectively demonstrate that GP-GL@Ca-E hydrogels exhibit excellent biocompatibility.

Cell Migration and in vitro Angiogenesis Analysis of GP-GL@Ca-E Hydrogels

The scratch assay was employed to evaluate the migratory capacity of HUVECs under hydrogel treatment (Figure 5G). Quantitative analysis at 48 h (Figure 5H) revealed that the hypoxia/high glucose model group exhibited a migration rate of 40.88%, while treatment with various hydrogel formulations significantly enhanced this rate. Notably, the GP-GL @Ca-E group demonstrated the most pronounced improvement, achieving a migration rate of 66.13%, approaching the normal group's rate of 76.72%. Neovascularization is a critical determinant of effective wound healing.[24] To assess the angiogenic potential of GP-GL@Ca-E in vitro, HUVECs were cultured with extracts from GP, GP-GL, and GP-GL@Ca-

https://doi.org/10.2147/IJN.S556446

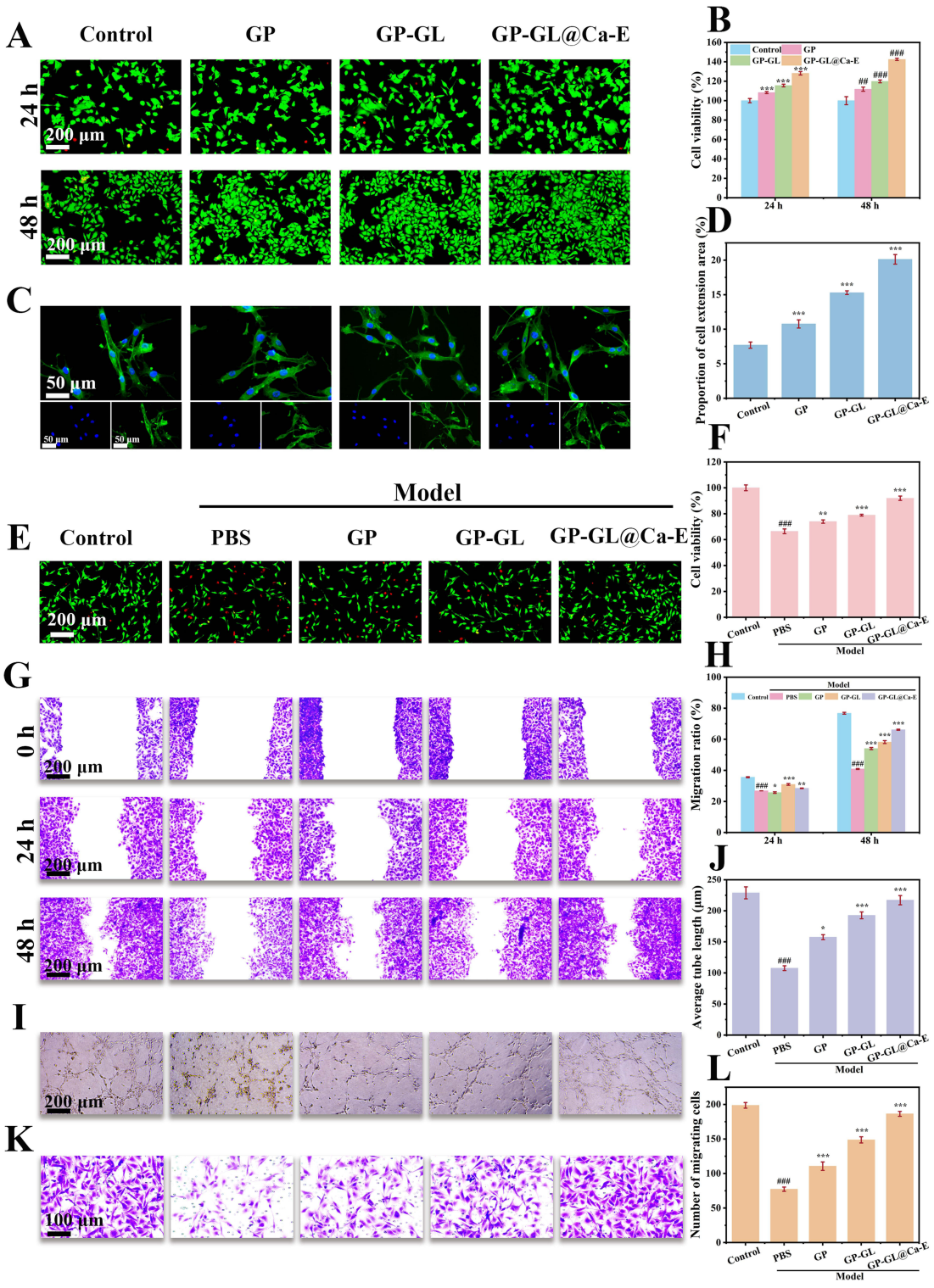

Figure 5 GP-GL@Ca-E hydrogel biocompatibility, cell migration, and in vitro angiogenesis analysis. (**A**) Live/dead fluorescence staining of HUVECs co-cultured with extracts from different-component hydrogels for 24 h and 48 h, and (**B**) quantifying cell viability. (**C**) Fluorescence images of cytoskeletal staining and (**D**) quantification of cell spreading area for HUVECs co-cultured with extracts from different-component hydrogels for 24 h. (**E**) Live/dead fluorescence staining and (**F**) CCK-8 assay quantifying cell viability for HUVECs (modeled under HG/hypoxic conditions) co-cultured with extracts from different-component hydrogels for 24 h. (**G**) Scratch assay and (**H**) quantitative results for HUVECs (modeled under HG/hypoxic conditions) treated with different-component hydrogels. (**I**) Tube formation assay at 12 h and (**J**) quantitative data of tube length for HUVECs (modeled under HG/hypoxic conditions) treated with different-component hydrogels. (**K**) Transwell assay assessing migration capacity and (**L**) quantification of migrated HUVECs (modeled under HG/hypoxic conditions) treated with different-component hydrogels. (# indicates compared to the Control group and * compared to the PBS group. ##p<0.01, and ####p<0.001; *p<0.05, **p<0.01, and ***p<0.001).

E hydrogels, and tubular structure formation was analyzed (Figure 5I). The HG model group showed significantly reduced nodes, branches, and tube length compared to the normal group, but these parameters were partially restored after hydrogel treatment. Quantitative analysis of tube length confirmed that GP-GL@Ca-E markedly promoted vascular network formation (Figure 5J). Further evaluation of cell recruitment via a 24 h Transwell assay (Figure 5K and L) demonstrated impaired recruitment in the hypoxia/high glucose model group, which was ameliorated by hydrogel treatment, with GP-GL@Ca-E exhibiting the most robust recovery, comparable to the normal group. Previous studies suggest that EGCG accelerates epithelial healing by upregulating bFGF expression in epithelial cells.[25] The migration and tubulation results indicate that EGCG retains its bioactivity and structural integrity after encapsulation and release from the hydrogel, preserving its original biological functions. Collectively, the GP-GL@Ca-E hydrogel system, with its encapsulated EGCG, demonstrates significant potential for tissue regeneration by effectively enhancing cell migration and angiogenesis.

ROS Scavenging and Anti-Inflammatory Effects of GP-GL@Ca-E Hydrogels in vitro

The diabetic wound microenvironment, characterized by elevated ROS levels and hypoxia, significantly impairs cell survival and proliferation.[26] Addressing this challenge, GP-GL@Ca-E hydrogels serve as ROS-driven oxygenators, eliminating ROS and supplying O_2 to restore microenvironmental balance. Their dual action in ROS scavenging and oxygen production was evaluated with the ROS probe DCFH-DA and oxygen sensor $Ru(dpp)_3Cl_2$. Results in Figure 6A reveal that HUVECs co-cultured with these hydrogels displayed a significant reduction in green fluorescence intensity compared to the PBS-treated model group, matching the low ROS levels seen in the Control group. Hypoxic conditions in the high glucose/hypoxia model group were confirmed by intense red fluorescence after $Ru(dpp)_3Cl_2$ staining, while GP-GL@Ca-E hydrogels effectively quenched this signal through oxygen generation from CaO_2 hydrolysis (Figure 6B).

Elevated ROS levels influence macrophage polarization, delaying wound healing,[27] whereas M2 macrophage polarization promotes diabetic wound repair through anti-inflammatory cytokine secretion.[28] Immunofluorescence analysis of macrophage surface markers (CD86 for M1, CD206 for M2) revealed that LPS-induced inflammatory models showed elevated CD86 expression compared to normal controls. Hydrogel treatments progressively reduced CD86 while increasing CD206 expression, with GP-GL@Ca-E demonstrating the most pronounced effect in promoting M2 polarization (Figure 6C and Figure S3). RT-PCR analysis of RAW264.7 cells showed LPS-induced M1 polarization through upregulated iNOS expression, while Arg-1 (M2 marker) remained unchanged. Hydrogel treatments reversed this trend, gradually decreasing iNOS and increasing Arg-1 expression (Figure 6D and E). Furthermore, inflammatory chemokines CCL2 and CXCL2 were assessed, with LPS stimulation significantly elevating both markers. CCL2 recruits circulating monocytes that differentiate into macrophages at inflammatory sites, creating a positive feedback loop that amplifies inflammation.[29] GP-GL@Ca-E hydrogel treatment normalized CCL2 levels (Figure 6F) and similarly modulated CXCL2 expression (Figure 6G), which mediates neutrophil infiltration and protease-mediated tissue damage.[30] These results demonstrate that GP-GL@Ca-E hydrogels exert anti-inflammatory effects through ROS scavenging, M2 macrophage polarization, and regulation of chemokine-mediated immune cell recruitment.

Acceleration of Diabetic Wound Healing and Histopathological Evaluation by GP-GL@Ca-E Hydrogels

Evaluating GP-GL@Ca-E hydrogel efficacy, diabetic rats (induced by single high-dose STZ i.p., blood glucose >16.7 mmol/L) received a 15-mm dorsal circular full-thickness excisional wound. The wound was then dressed with GP, GP-GL, or GP-GL @Ca-E hydrogel. As shown in Figure 7A and B, wound areas were photographed at specific intervals to compare healing rates. After 14 days of treatment, the GP-GL@Ca-E group exhibited nearly complete wound closure (99.01%), while the model group retained unhealed regions (86.32%), demonstrating the superior efficacy of GP-GL@Ca-E hydrogels in accelerating diabetic wound healing. Notably, both GP and GP-GL hydrogels also promoted wound closure compared to the model, likely attributable to their ability to provide a moist healing environment and barrier against bacterial infection.[31] Histological analysis via H&E and Masson staining was performed on days 7 and 14 post-treatment (Figure 7C). On day 7, all groups displayed varying degrees of inflammation, but by day 14, the model group still exhibited pronounced inflammatory infiltration, whereas the GP-GL@Ca-E

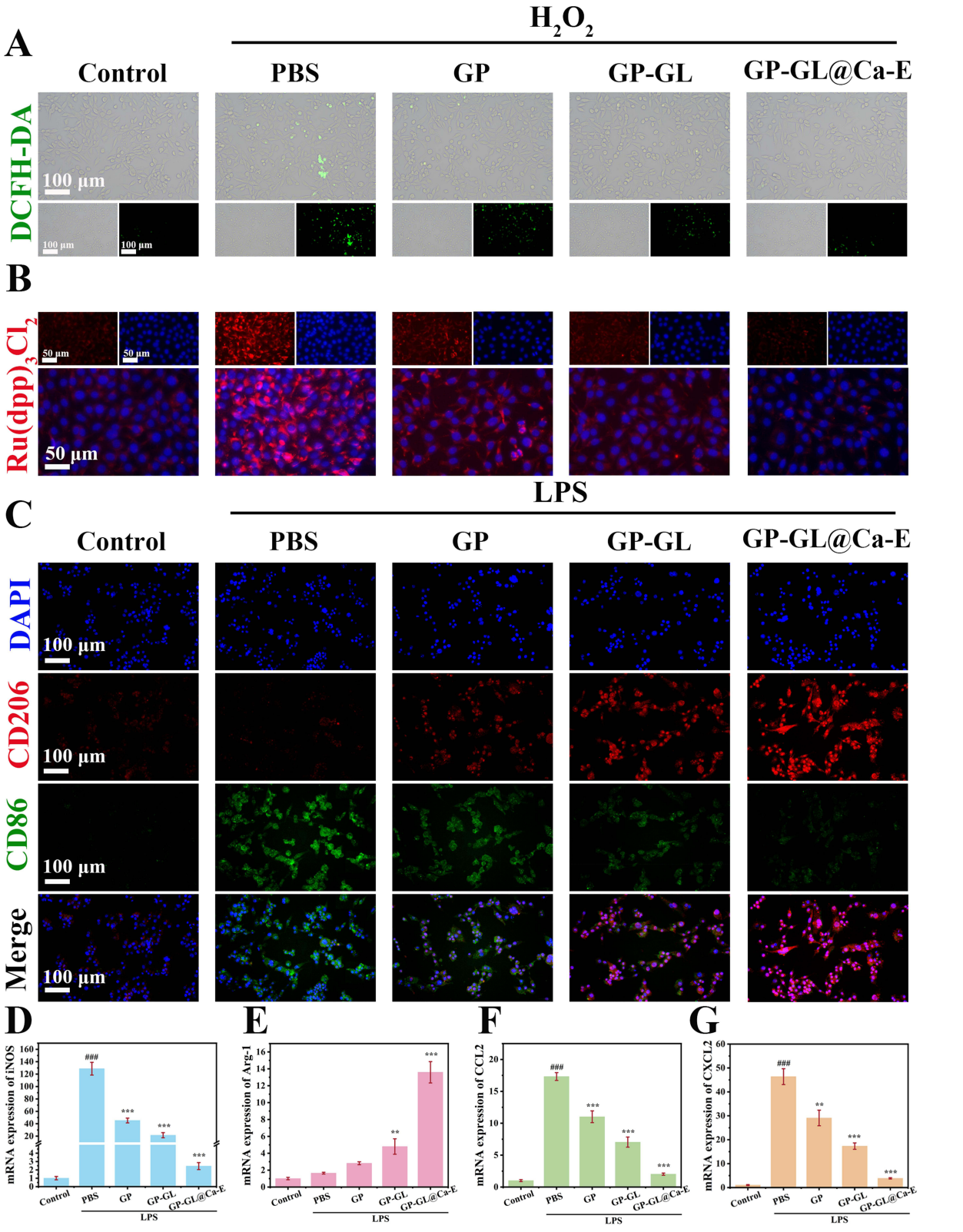

Figure 6 ROS scavenging and anti-inflammatory effects of GP-GL@Ca-E hydrogels in vitro. (**A**) Intracellular ROS levels in cells treated with different-component hydrogels, determined using the ROS-specific probe DCFH-DA. (**B**) Oxygen generation capacity of cells treated with different-component hydrogels, assessed using the oxygen indicator $Ru(dpp)_3Cl_2$. (**C**) Macrophage polarization status following treatment with different-component hydrogels, evaluated by immunofluorescence staining. mRNA expression levels of (**D**) iNOS, (**E**) Arg-1, (**F**) CCL2, and (**G**) CXCL2 detected by qPCR. (# indicates compared to the Control group and * compared to the PBS group. ###p<0.001; **p<0.01, and ***p<0.001).

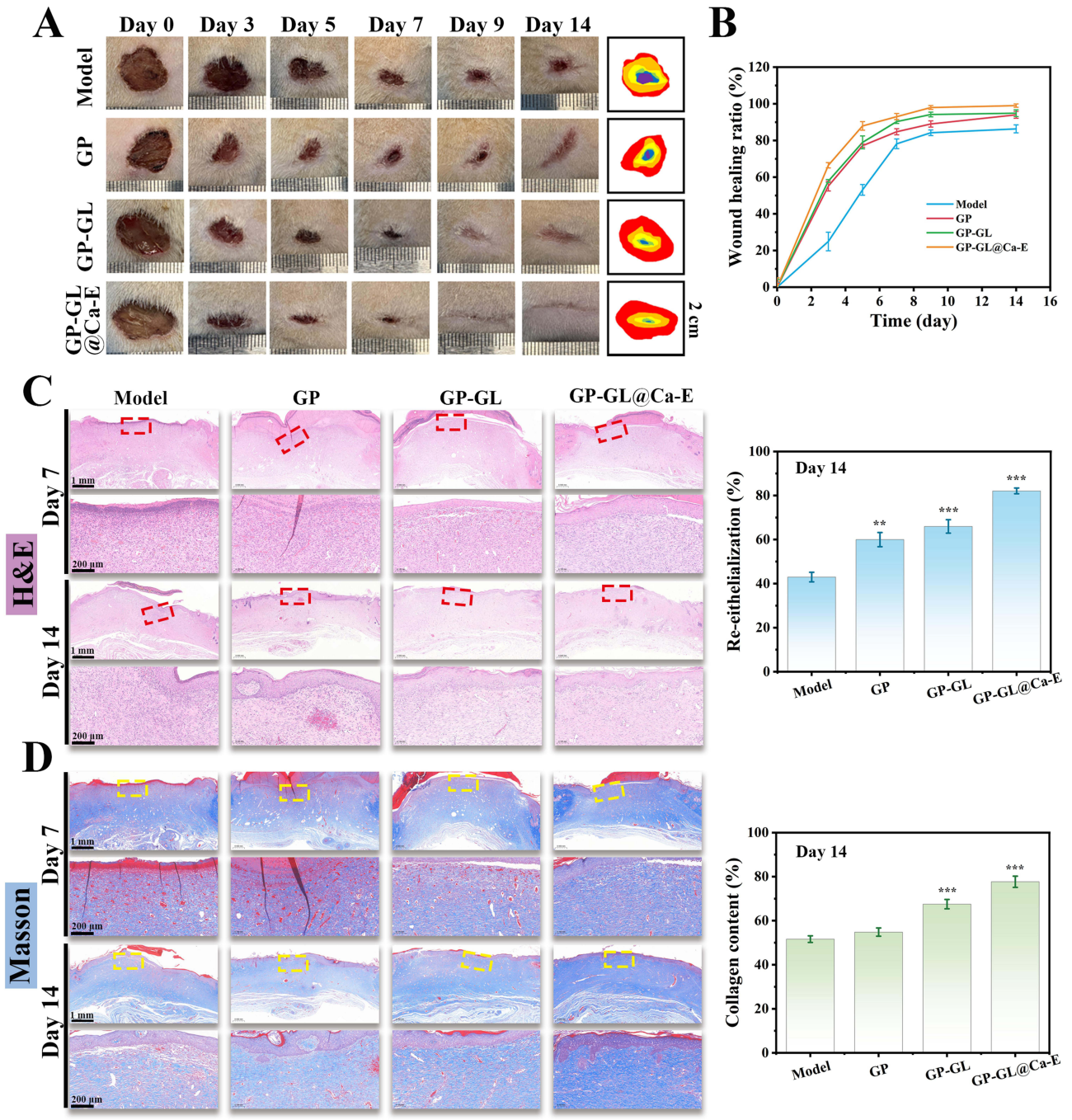

Figure 7 Acceleration of diabetic wound healing and histopathological evaluation by GP-GL@Ca-E hydrogels. (**A**) Wound images and wound area overlays at indicated time points. (**B**) Quantitative analysis of wound healing rate. Skin tissue sections stained with (**C**) H&E and (**D**) Masson's trichrome. (* indicates compared to the Model group. **p<0.01, and ***p<0.001).

group showed resolved inflammation, increased epithelial thickness, and enhanced hair follicle formation, along with denser granulation tissue. Collagen, a critical component for tissue regeneration,[32] was assessed as an indicator of skin repair. Masson staining (Figure 7D) revealed a gradual shift from red to blue in hydrogel-treated groups by day 7, indicating progressive collagen deposition. By day 14, the GP-GL@Ca-E group demonstrated denser and more organized collagen fibers, confirming its ability to significantly improve collagen remodeling at the wound site. These findings collectively demonstrate that GP-GL@Ca-E hydrogels accelerate diabetic wound healing by enhancing re-epithelialization and collagen deposition in damaged tissue.

https://doi.org/10.2147/IJN.S556446

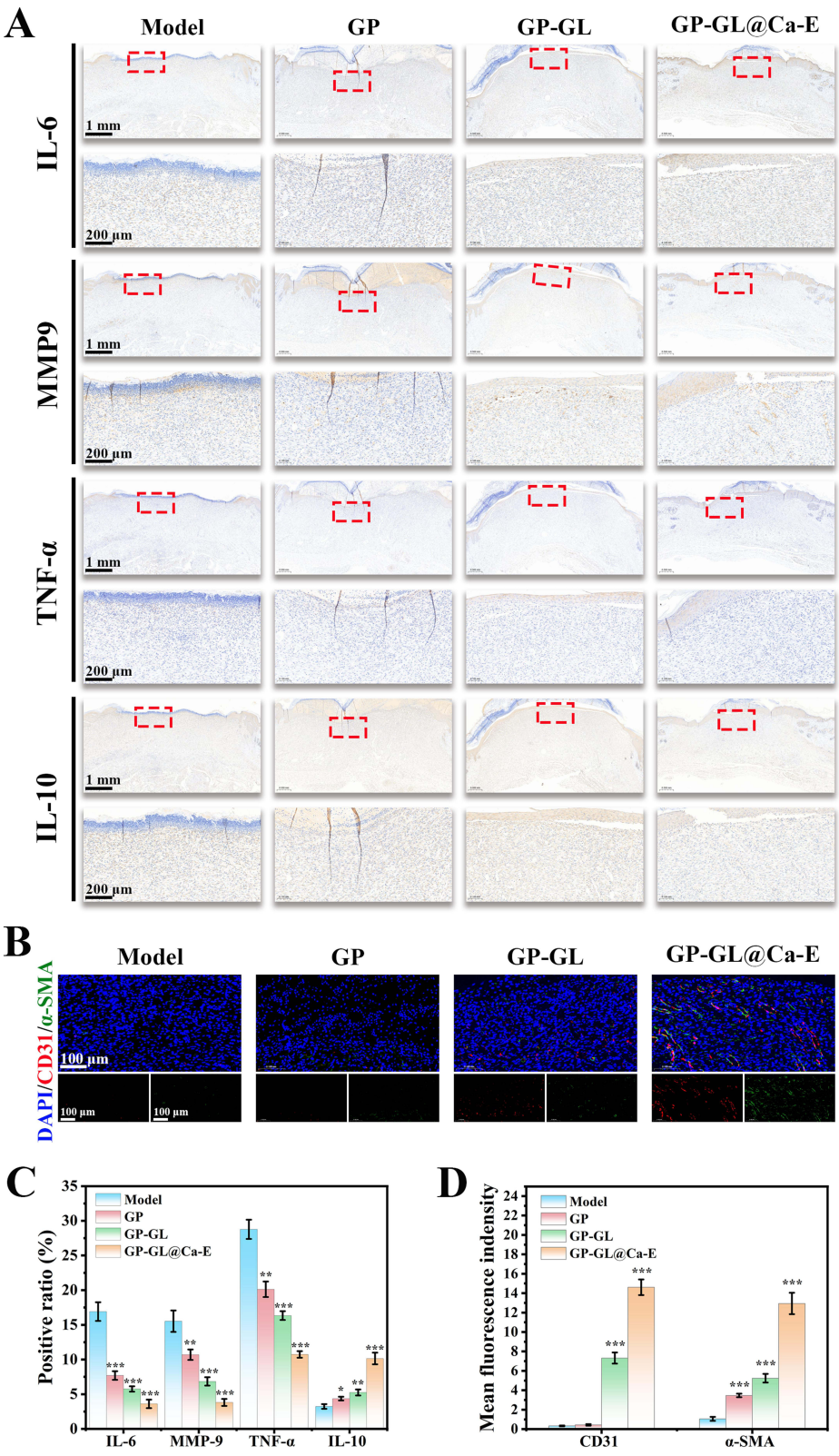

Figure 8 Modulation of inflammatory response and promotion of angiogenesis by GP-GL@Ca-E hydrogels in vivo. (**A**) IHC for IL-6, MMP9, TNF-α, IL-10 and (**B**) IF for CD31, α-SMA in day 7 skin tissues. (**C**) Percentage of positive cells for the four proteins tested by IHC. (**D**) Quantitative analysis of CD31 and α-SMA fluorescence. (* indicates compared to the Model group. $^{**}p<0.01$, and $^{***}p<0.001$).

Modulation of Inflammatory Response and Promotion of Angiogenesis by GP-GL@Ca-E Hydrogels in vivo

Cytokines play pivotal roles in wound repair processes, serving as key molecular indicators of tissue regeneration progress. Previous studies have demonstrated that hyperglycemia and oxidative stress in diabetic wounds lead to sustained upregulation of MMP9 expression, which promotes excessive ECM degradation and impairs granulation tissue formation, thereby maintaining a chronic inflammatory state.[33,34] To evaluate the inflammatory microenvironment, immunohistochemical staining was performed for IL-6, MMP9, TNF-α, and IL-10. As shown in Figure 8A and C, untreated model group wounds exhibited high expression of pro-inflammatory cytokines (IL-6, MMP9, and TNF-α) at day 7 post-injury. In contrast, hydrogel-treated groups showed reduced pro-inflammatory marker expression, with GP-GL@Ca-E demonstrating the most significant suppression of inflammatory cytokines and the highest induction of anti-inflammatory IL-10, attributable to its combined antimicrobial and antioxidant properties. Angiogenesis, critical for chronic wound healing,[35] was assessed through CD31 and α-SMA immunofluorescence (Figure 8B and D). While model group wounds displayed limited CD31 expression at day 7, GP-GL@Ca-E treatment significantly enhanced CD31 levels, indicating robust neovascularization. This effect stems from dual mechanisms: oxygen generation by CaO_2[36] and EGCG-mediated VEGF upregulation.[37] Additionally, α-SMA expression, which confers contractile capacity to myofibroblasts for wound contraction,[38] was markedly increased in GP-GL@Ca-E-treated wounds compared to model group, further confirming its therapeutic efficacy. These collective findings demonstrate that GP-GL@Ca-E hydrogels effectively mitigate diabetic wound inflammation through cytokine modulation while promoting tissue repair via enhanced angiogenesis and myofibroblast activation.

Conclusion

This study successfully developed a multifunctional hydrogel delivery system (GP-GL@Ca-E) based on dual responsiveness to ROS and glucose, demonstrating significant potential for application in diabetic wound management. The system was constructed by encapsulating the oxygen-generating component, calcium peroxide (CaO_2), within the core of QP, followed by anchoring EGCG onto the QP surface via dynamic borate bonds, thereby forming functionalized nanoparticles. Subsequently, these nanoparticles were integrated into a double-network hydrogel matrix. Within the diabetic wound microenvironment, elevated levels of ROS and glucose trigger the cleavage of borate bonds, enabling the controlled release of EGCG. This effectively scavenges excess ROS and mitigates oxidative stress damage. Following the release of EGCG, CaO_2 reacts with water to continuously release O_2, significantly alleviating local hypoxia at the wound site. The functionalized gelatin matrix (GP/GL), upon UV-crosslinking, forms an in situ hydrogel dressing that conforms to irregular wound beds, providing appropriate mechanical support and maintaining a moist healing microenvironment, while exhibiting good biocompatibility. In a rat model of diabetic full-thickness skin defects, the GP-GL@Ca-E hydrogel effectively remodeled the wound microenvironment by promoting collagen deposition, suppressing inflammatory responses, and accelerating neovascularization, leading to a significantly accelerated wound healing process. In conclusion, this work provides a novel therapeutic strategy with substantial clinical application prospects for chronic diabetic wounds.

Data Sharing Statement

The data that support the findings of this study are available from the corresponding author upon reasonable request.

Acknowledgments

This work was supported by the Medical Scientific Research Foundation of Guangdong Province, China (B2024129), Administration of Traditional Chinese Medicine of Guangdong Province, China (20251012), Science and Technology Program of Guangzhou, China (2025A04J4039) and Guangzhou Municipal Science and Technology Plan Project: City-University (Institution)-Enterprise Joint Funding (2025A03J4516).

Disclosure

The authors declare no conflicts of interest in this work.

References

1. Peña OA, Martin P. Cellular and molecular mechanisms of skin wound healing. *Nat Rev Mol Cell Biol*. 2024;25(8):599–616. doi:10.1038/s41580-024-00715-1
2. Sun H, Saeedi P, Karuranga S, et al. IDF Diabetes Atlas: global, regional and country-level diabetes prevalence estimates for 2021 and projections for 2045. *Diabet Res Clin Pract*. 2022;183:109119. doi:10.1016/j.diabres.2021.109119
3. Uberoi A, McCready-Vangi A, Grice EA. The wound microbiota: microbial mechanisms of impaired wound healing and infection. *Nat Rev Microbiol*. 2024;22(8):507–521. doi:10.1038/s41579-024-01035-z
4. Liu Z, Bian X, Luo L, et al. Spatiotemporal single-cell roadmap of human skin wound healing. *Cell Stem Cell*. 2025;32(3):479–498. doi:10.1016/j.stem.2024.11.013
5. Chang M, Nguyen TT. Strategy for Treatment of Infected Diabetic Foot Ulcers. *Acc Chem Res*. 2021;54(5):1080–1093. doi:10.1021/acs.accounts.0c00864
6. Xiong Y, Mi BB, Lin Z, et al. The role of the immune microenvironment in bone, cartilage, and soft tissue regeneration: from mechanism to therapeutic opportunity. *Mil Med Res*. 2022;9(1):65. doi:10.1186/s40779-022-00426-8
7. Xiong Y, Mi BB, Shahbazi MA, et al. Microenvironment-responsive nanomedicines: a promising direction for tissue regeneration. *Mil Med Res*. 2024;11(1):69. doi:10.1186/s40779-024-00573-0
8. Kim HS, Sun X, Lee JH, et al. Advanced drug delivery systems and artificial skin grafts for skin wound healing. *Adv Drug Deliv Rev*. 2019;146:209–239. doi:10.1016/j.addr.2018.12.014
9. Frykberg RG, Banks J. Challenges in the Treatment of Chronic Wounds. *Adv Wound Care*. 2015;4(9):560–582. doi:10.1089/wound.2015.0635
10. Dinh T, Tecilazich F, Kafanas A, et al. Mechanisms involved in the development and healing of diabetic foot ulceration. *Diabetes*. 2012;61(11):2937–2947. doi:10.2337/db12-0227
11. Dasari N, Jiang A, Skochdopole A, et al. Updates in Diabetic Wound Healing, Inflammation, and Scarring. *Semin Plast Surg*. 2021;35(3):153–158. doi:10.1055/s-0041-1731460
12. Costa PZ, Soares R. Neovascularization in diabetes and its complications. Unraveling the angiogenic paradox. *Life Sci*. 2013;92(22):1037–1045. doi:10.1016/j.lfs.2013.04.001
13. Okonkwo UA, DiPietro LA. Diabetes and Wound Angiogenesis. *Int J Mol Sci*. 2017;18(7). doi:10.3390/ijms18071419
14. Desmet CM, Préat V, Gallez B. Nanomedicines and gene therapy for the delivery of growth factors to improve perfusion and oxygenation in wound healing. *Adv Drug Deliv Rev*. 2018;129:262–284. doi:10.1016/j.addr.2018.02.001
15. Sforna L, Cenciarini M, Belia S, et al. The role of ion channels in the hypoxia-induced aggressiveness of glioblastoma. *Front Cell Neurosci*. 2014;8:467. doi:10.3389/fncel.2014.00467
16. Wang Z, Feng C, Lu S, et al. Nanoscale CaO(2)-Loaded Surface-Engineered Iodine-125 Seed with Sustained Self-Oxygenation for Sensitized Tumor Brachytherapy. *Small*. 2025;21(14):e2411193. doi:10.1002/smll.202411193
17. Gao C, Huang Y, Zhang L, et al. Self-reinforcement hydrogel with sustainable oxygen-supply for enhanced cell ingrowth and potential tissue regeneration. *Biomater Adv*. 2022;141:213105. doi:10.1016/j.bioadv.2022.213105
18. Bankar N, Latta L, Loretz B, et al. Antimicrobial and antibiotic-potentiating effect of calcium peroxide nanoparticles on oral bacterial biofilms. *NPJ Biofilms Microbiomes*. 2024;10(1):106. doi:10.1038/s41522-024-00569-7
19. Jia L, Zhou Z, Li X, et al. A multifunctional ROS cascade nanoplatform enables common prosperity of O2 and H2O2 for magnetic targeting and fluorescence imaging-guided photodynamic/chemodynamic therapy. *Chem Eng J*. 2025;506:160178.
20. He X, Gao Y, Wang X, et al. Dual-network hydrogel loaded with antler stem cells conditioned medium and EGCG promotes diabetic wound healing through antibacterial, antioxidant, anti-inflammatory, and angiogenesis. *Mater Today Bio*. 2025;31:101612. doi:10.1016/j.mtbio.2025.101612
21. Wang Y, Zhu Z, Lv X, et al. Multifunctional carboxymethyl chitosan-based sponges loaded with epigallocatechin-3-gallate for accelerating wound healing in diabetic rats with full-thickness burns. *Carbohydr Polym*. 2025;350:123025.
22. Guo Z, Yan L, Zhou B, et al. In situ photo-crosslinking silk fibroin based hydrogel accelerates diabetic wound healing through antibacterial and antioxidant. *Int J Biol Macromol*. 2023;242(Pt 3):125028. doi:10.1016/j.ijbiomac.2023.125028
23. Li J, Wang M, Tan X, et al. A dual-component particulate dressing for simultaneous microenvironment modulation and tissue regeneration in infected diabetic wounds. *Mater Today Bio*. 2025;33:102005.
24. Kim J, Bong KW, Cho JK, et al. Thermo-responsive hydrogel via sustained Co-delivery of TA and PDGF to modulate the diabetic microenvironment and accelerate diabetic wound healing. *J Mater Chem B*. 2025;13(24):7090–7105. doi:10.1039/d5tb00563a
25. Xu S, Chang L, Hu Y, et al. Tea polyphenol modified, photothermal responsive and ROS generative black phosphorus quantum dots as nanoplatforms for promoting MRSA infected wounds healing in diabetic rats. *J Nanobiotechnol*. 2021;19(1):362. doi:10.1186/s12951-021-01106-w
26. Li Z, Zhao Y, Huang H, et al. A Nanozyme-Immobilized Hydrogel with Endogenous ROS-Scavenging and Oxygen Generation Abilities for Significantly Promoting Oxidative Diabetic Wound Healing. *Adv Healthc Mater*. 2022;11(22):e2201524. doi:10.1002/adhm.202201524
27. Jin N, Wang Z, Tang X, et al. Promoting Diabetic Wound Healing through a Hydrogel-Based Cascade Regulation Strategy of Fibroblast-Macrophage. *Adv Healthc Mater*. 2024;13(16):e2400526. doi:10.1002/adhm.202400526
28. Xiong Y, Lin Z, Bu P, et al. A Whole-Course-Repair System Based on Neurogenesis-Angiogenesis Crosstalk and Macrophage Reprogramming Promotes Diabetic Wound Healing. *Adv Mater*. 2023;35(19):e2212300. doi:10.1002/adma.202212300
29. Wang Y, Wang G, Li J, et al. CCL2-scavenging nanodecoy hydrogel multi-step remodel monocytes recruitment and macrophages polarization for periodontitis treatment. *Chem Eng J*. 2024;501:157660.
30. De filippo K, Dudeck A, Hasenberg M, et al. Mast cell and macrophage chemokines CXCL1/CXCL2 control the early stage of neutrophil recruitment during tissue inflammation. *Blood*. 2013;121(24):4930–4937. doi:10.1182/blood-2013-02-486217
31. Zhang Y, Wu H, Li P, et al. Dual-Light-Triggered In Situ Structure and Function Regulation of Injectable Hydrogels for High-Efficient Anti-Infective Wound Therapy. *Adv Healthc Mater*. 2022;11(1):e2101722. doi:10.1002/adhm.202101722

32. Du B, Ren X, Wang X, et al. Four-in-one pH/glucose-responsive engineered hydrogel for diabetes wound healing. *Nano Today*. 2025;62:102725.
33. Wang J, Zhang H, Hu S, et al. A MMP9-responsive nanozyme hydrogel to promote diabetic wound healing by reconstructing the balance of pro-inflammation and anti-inflammation. *J Mater Chem B*. 2025. doi:10.1039/d4tb02857k
34. Neuhoferova E, Kindermann M, Buzgo M, et al. Topical siRNA therapy of diabetic-like wound healing. *J Mater Chem B*. 2025;13(3):1037–1051. doi:10.1039/d4tb01547a
35. Liu L, Zheng CX, Zhao N, et al. Mesenchymal Stem Cell Aggregation-Released Extracellular Vesicles Induce CD31(+) EMCN(+) Vessels in Skin Regeneration and Improve Diabetic Wound Healing. *Adv Healthc Mater*. 2023;12(20):e2300019. doi:10.1002/adhm.202300019
36. Ullah A, Zaidi MB, Mamun AA, et al. A visible light crosslinked angiogenic and anti-inflammatory GelMA microneedle array patch co-releasing nitric oxide and oxygen for diabetic wound healing. *Int J Biol Macromol*. 2025;319(Pt 2):145450. doi:10.1016/j.ijbiomac.2025.145450
37. Yin X, Huang S, Xu S, et al. Preparation of pro-angiogenic, antibacterial and EGCG-modified ZnO quantum dots for treating bacterial infected wound of diabetic rats. *Biomater Adv*. 2022;133:112638. doi:10.1016/j.msec.2021.112638
38. McAndrews KM, Miyake T, Ehsanipour EA, et al. Dermal αSMA(+) myofibroblasts orchestrate skin wound repair via β1 integrin and independent of type I collagen production. *EMBO J*. 2022;41(7):e109470. doi:10.15252/embj.2021109470